Non-invasive In-line Food Inspection via Microwave Imaging Technology

Jorge A. Tobon Vasquez, *Member, IEEE*, Rosa Scapaticci, *Member, IEEE*, Giovanna Turvani, Marco Ricci, *Member, IEEE*, Laura Farina, *Member, IEEE*, Amelie Litman, *Member, IEEE*, Mario R. Casu, *Senior Member, IEEE*, Lorenzo Crocco, *Senior Member, IEEE* and Francesca Vipiana, *Senior Member, IEEE*.

***Abstract*—Contamination with foreign objects is one of the main causes of costumers' complaint against food manufacturers. Although different technologies are used for food/beverage in-line monitoring, several cases of contaminated food products are still reaching the market, above all with plastic and glass fragments. In this work, we propose the use of a microwave imaging technology to monitor packaged food along the production line. In this framework, microwave imaging exploits the differences in dielectric properties between the food and the contaminant as well as the differences between faulty and unaltered items. A dedicated microwave imaging system is firstly designed and validated through numerical simulations. Then, the realized prototype device is assessed experimentally, both in controlled laboratory conditions and along an industrial production line. The outcomes of this study show the capabilities of this technology for food safety and security.**

***Index Terms*—Microwave imaging, non-invasive diagnostics, food inspection, food security, food safety.**

I. Introduction

In food industry, foreign body contamination, packaging failures, or items with poor characteristics (texture, appearance) are among the main sources of costumers' complaint against manufacturers, resulting in loss of brand loyalty and large recall expenses. To cope with these issues, technologies such as metal detectors (MD), X-ray (XRI) and near infrared (NIR) imaging are currently adopted in food industry for monitoring food quality and safety. However, the occurrence of incidents remains significant, as each of these technologies have some limitations. For instance, MD can only detect metallic objects, whereas XRI cannot easily recognize low-density foreign objects such as most plastics and thin glass (which are the most common type of contaminants) and it can be harmful for operators accidentally exposed to its radiation. Finally, NIR techniques are rapid and safe but limited by the short penetrating length and the strong absorption in water. For these reasons, none of the technologies currently adopted can address all the requirements of food-industry and so there is an interest in developing novel technologies to address these issues that can be complementary to the ones already available along food packaging lines. Such a new technology for food quality and safety should be easy to use (to avoid the need of a team of specialized technicians), contact-less and with low impact on the food production chain (to avoid high installation costs), rapid and with high-throughput for in-line food monitoring, as well as low-cost (to be adopted both by large and small enterprises).

Among the possible candidates, electromagnetic (EM) sensing technologies represent an attractive, cost-effective option. In fact, most important characteristics of food products that affect their quality (e.g., water content, presence of contaminants) have also a direct influence on their EM properties and can be thus detected by EM devices.

In the last years, EM radiations at THz frequencies have been proposed for food inspection, also at industrial level [1]–[4]. THz systems are used to detect superficial defects, e.g. in the packaging, but are not the winning technology for detecting possible contaminants hidden inside food products, due to the intrinsic limited penetration of THz radiation. Moreover, the potential of THz technologies in food inspection is still at its early stage and far to be completely assessed.

Recently, there has been an interest in microwave imaging (MWI) for food quality and safety assessment [5]–[7]. MWI exploits the differences in dielectric properties of materials. The object under analysis is illuminated with low-power waves at microwave frequencies, radiated by a set of antennas placed at some distance from it. The resulting scattered EM waves are recorded by the same antennas and processed with suitable algorithms to translate them into an image of the targets.

Differently from THz radiations microwaves can penetrate objects up to some centimeters, making them suitable for monitoring packaged food. Penetration in both cases has to be considered only for non-metallic packaging. Hence, MWI can be used for in-line detection of foreign body contaminants in food products along the production chain. In particular, MWI can be exploited for the detection of contaminants that are not easily visible with XRI systems due their low density contrast with the surrounding medium, such as plastics and thin glass

Manuscript received XXX, 2020; accepted XXX. Date of publication XXX; date of current version XXX. This work was supported by Compagnia di San Paolo, under the research project "MIT-Food, Microwave Imaging Technology for Food Contamination Monitoring", and by the Italian Ministry of University and Research under the PRIN project "BEST-Food, Broadband Electromagnetic Sensing Technologies for Food quality and security assessment". *(Corresponding author: Francesca Vipiana)*

J. A. Tobon Vasquez, G. Turvani, M. Ricci, M. R. Casu and F. Vipiana are with the Department of Electronics and Telecommunications, Politecnico di Torino, 10129 Torino, Italy (e-mail: francesca.vipiana@polito.it).

R. Scapaticci and L. Crocco are with the Institute for the Electromagnetic Sensing of the Environment, National Research Council of Italy, 80124 Napoli, Italy (e-mail: crocco.l@irea.cnr.it).

L. Farina was with the Department of Electronics and Telecommunications, Politecnico di Torino, 10129 Torino, Italy. She is now with the Translational Medical Device Lab at the National University of Ireland, Galway, Ireland (e-mail: laura.farina@nuigalway.ie).

A. Litman is with Aix Marseille Univ., CNRS, Centrale Marseille, Institut Fresnel, Marseille, France, France (e-mail: amelie.litman@fresnel.fr).

fragments or bone and cartilage splinters in meat and poultry products, as well as in fish [8]. Another prospective application is the detection of insects and pests in fruits and vegetables [8], which is currently done via visual inspection, with obvious drawbacks in terms of cost, time and failures. Besides quality control applications, MWI based technology could also serve as security monitoring technology against intentional product alterations. Indeed, a non-destructive characterization of the dielectric properties of wet products could help assessing their safe or threatening nature. However, to date, only a limited literature is available on this topic and it deals essentially with non-imaging devices [9] and radar-based techniques for food screening [10]. Still no experiment or feasibility study has been reported to support the concept.

In this paper, we describe the design, realization and testing of a novel MWI-based prototype device for the detection of foreign contaminants in packaged food moving along the production line, and we face the problem of detecting plastic or glass fragments into homogeneous food hosted in a plastic or glass jar. Given the great variability of food-industry products, we focus on a specific case study, that is detecting contaminant fragments into hazelnut-cocoa cream in a glass jar. However, MWI technology is viable also for other food products, provided that the main system requirements (working frequency, measurement sampling, etc.) are designed accordingly.

The key idea underlying the developed methodology and device is that items moving along the production chain are almost exactly identical. This allows to adopt a differential imaging approach, where data from a "reference" item are subtracted from data related to the product under test. Then, it is possible to detect contaminants, accidentally fallen inside the packaged food product, via the processing of the measured differential data. The data from the "reference" item could be gathered once via a specific measurement, stored and compared with the current measurements. Another, possibly more feasible, option is to take the differential data as the difference of measurements taken on sequential food products and then, assuming that the presence of contaminants is a rare event, discard the pair of products that generate an image with the presence of the contaminant(s).

The relative movement of the object under test with respect to the measurement devices represents the key of the developed system. As detailed in the following, the movement allows to increase the available information content of the measured data by taking advantage of different directions under which the moving target is seen from the antennas. Accordingly, the resulting microwave imaging algorithm exploits a "synthetic aperture" approach, in which the data are acquired for different positions of the target and, then, joined together by means of a proper "model-based" procedure. On the other hand, the movement of the target poses well-defined limits and constraints on the way in which the imaging system can operate, in terms of number of possible measurements, measurement configurations, speed of acquisition and processing. Preliminary feasibility studies of the proposed MWI system are reported in [11]–[14].

The paper is structured as follows. The design and architecture of the proposed MWI system is detailed in Sect. II.

Fig. 1. Example of a food packaging line (photo available in https://www.nutkao.com/en/album/nutkao-italy/).

Section III describes the initial system validation in a 2-D simplified simulated scenario. Sect. IV presents the 3-D imaging results for an experiment testing the realized system in a controlled environment. Section V reports the results of a measurement campaign performed at an industrial facility. Finally, conclusions and perspectives are given in Sect. VI.

II. Microwave Imaging System Design

An example of a food packaging line is shown in Fig. 1. It is evident that to perform in-line food monitoring several constraints have to be taken into account to design an MWI system suitable to perform this task. First of all, both measurements and data processing have to be performed in a very short time because the food products move on a high speed conveyor belt (e.g. in the example of Fig. 1 the speed is 3 jars per second). Moreover, the sensors can be placed only at the two sides of the conveyor belt, so that only aspect-limited measurements are possible (i.e., it is not possible to probe the target from all possible view angles). Finally, the guides along the conveyor belt are made of stainless steel, that strongly interacts with microwave fields and it has to be properly modeled during the system design. In the following sub-sections, the proposed system architecture and configuration are described in detail, together with the kind of considered food products.

A. System Architecture

As previously mentioned, food products move on a high speed conveyor belt and measurements have to be performed without stopping or delaying it. This implies that the MWI system has to be designed with the aim of reducing its complexity as much as possible. Accordingly, two antennas are placed on the two opposite sides of the line [see Fig. 2.(a)]. The two antennas illuminate the region of interest and are connected to a vector network analyzer (VNA) that takes sequentially measurements of the 2×2 scattering matrix. Considering the movement of the monitored food product, each measurement is performed in a different relative position between the food product and the antennas. This configuration is fully equivalent to an array of antennas placed at both sides of the line while the food product is staying still in the middle, as shown in Fig. 2.(b), where the "virtual" antennas are

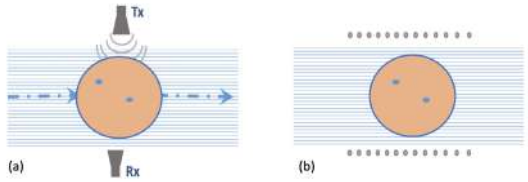

Fig. 2. Microwave imaging system concept; (a): food product (orange circle) moving along the line (dashed arrows) with two antennas at the two sides of the line; (b): equivalent configuration with two synthetic antenna arrays (grey dots) at the two sides of the line with the food product in the middle.

represented by grey dots. In the equivalent model, a sequence of 2×2 scattering matrices are measured, one for each facing pair of antennas.

The speed of the conveyor belt determines how many 2×2 scattering matrices can be measured with the VNA while the food product passes through the two antennas. In turn, the VNA measurement time is mainly related to the number of frequency points measured and to the bandwidth of the VNA intermediate frequency (IF) filter (a wider IF bandwidth allows faster measurement speed but increases the VNA noise floor, reducing the measurement accuracy).

To give an idea of the available measurement time, we consider the case reported in Fig. 1 where the belt speed is of 3 jars/s. Considering a jar diameter of 8 cm and an average spacing of 8 cm (equivalent to one jar) between two consecutive jars, the velocity of the line is 48 cm/s. Assuming a "measurement window" corresponding to the jar diameter plus 2 buffer zones of 2 cm each, before and after the considered jar (as shown in Fig. 3), the measurement window length is 12 cm. For a belt velocity of 48 cm/s, this corresponds to a measurement time per jar of 0.25 s. Then, the number of 2×2 scattering matrices which can be measured depends on the VNA performances in terms of sweep time. For example, the typical cycle time of the Keysight P9370A VNA is 19.7 ms, for the full frequency span up to 14 GHz with 201 sample points, the IF bandwidth being equal to 100 kHz, without calibration and including data transfer time [15]. Accordingly, up to 13 scattering matrices can be acquired with such a VNA (which is equivalently to having 13 antennas positioned on each side of the belt, as shown with grey dots in Fig. 3).

The presence of contaminants, such as fragments of plastic or glass, within the food product, is modelled with a variation of the electric contrast $\Delta\chi = (\epsilon_c - \epsilon_b)/\epsilon_b$, where ϵ_c and ϵ_b are the complex permittivity of the contaminant and of the food within the packaging (i.e. background medium), respectively. When the food product is illuminated, the presence of contaminants will lead to a variation of the measured scattering matrices.

From the imaging point of view, we can assume that the contaminant represents a *small* perturbation in an otherwise known scenario; hence, a *differential* imaging approach is a suitable choice [16], [17]. In particular, the input data of the imaging problem, denoted as ΔS in the following, are represented by the difference between the scattering parameters S measured for a given food product and the scattering parameters S_b measured for the "reference" food product, i.e.

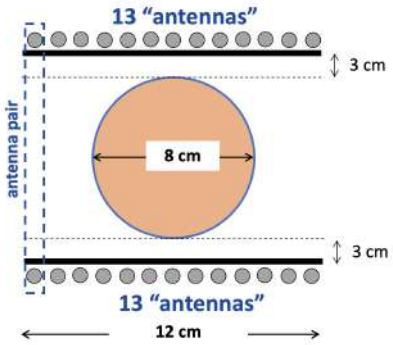

Fig. 3. Measurement window and position of the antennas forming the synthetic aperture.

the food product without the contaminant. The output is an image showing the variation of the electric contrast $\Delta\chi$ within the food product due to the contaminant.

Since the contrast variation $\Delta\chi$ is localized in a small portion of the imaging domain D, represented here by the content of the food product, it is possible to apply the so called distorted Born approximation [18], obtaining the following *linear* relationship between ΔS and $\Delta\chi$

$$\Delta S\left(\boldsymbol{r}_p, \boldsymbol{r}_q\right) = \mathbb{S}\left(\Delta\chi\right), \tag{1}$$

where $\mathbb{S}$ is a linear and compact integral operator, so that (1) casts a linear and ill-posed inverse problem. The kernel of $\mathbb{S}$ is $-j\omega\epsilon_b/4\, \boldsymbol{E}_\mathrm{b}\left(\boldsymbol{r}_m, \boldsymbol{r}_p\right) \cdot \boldsymbol{E}_\mathrm{b}\left(\boldsymbol{r}_m, \boldsymbol{r}_q\right)$, where "$\cdot$" denotes the dot product between vectors, $\omega = 2\pi f$ is the angular frequency and j the imaginary unit. Moreover, $\boldsymbol{r}_m$ is the position of a point within the imaging domain D (i.e., the jar), and $\boldsymbol{r}_p$ and $\boldsymbol{r}_q$ denote the positions of the transmitting and receiving antennas respectively, in this case each antenna pair on the two sides of the line. Finally, $\boldsymbol{E}_\mathrm{b}$ is the background field in the unperturbed scenario (the product without the contaminant), radiated inside the imaging domain by each antenna.

A well-known tool to solve (1) is the truncated singular value decomposition (TSVD) algorithm [18], in which the unknown differential contrast function is obtained through the regularized inversion formula

$$[\Delta\chi] = \sum_{n=1}^{T} \frac{1}{\sigma_n} \left\langle [\Delta S], [u_n] \right\rangle [v_n], \tag{2}$$

where $[\Delta\chi]$ and $[\Delta S]$ are vectors collecting the contrast variation at the M sample points $\boldsymbol{r}_m \in D$ and the N scattering parameters $\Delta S_{p,q}$, corresponding to the pairs of antennas located in $(\boldsymbol{r}_p, \boldsymbol{r}_q)$, at the N_f measured frequency points, respectively; $[u_n]$, $[v_n]$ and σ_n are the n-th left and right singular vectors and the n-th singular value of the $(N \cdot N_f) \times M$ discretized scattering operator $[\mathbb{S}]$. Finally, T is the truncation index, which acts as a regularization parameter, ruling the trade-off between stability and accuracy in the reconstructions [18]. It is worth noting that TSVD enables real time data processing, since the computational intensive parts of the algorithm (i.e. $[\mathbb{S}]$ matrix construction and computation of its SVD) can be performed offline.

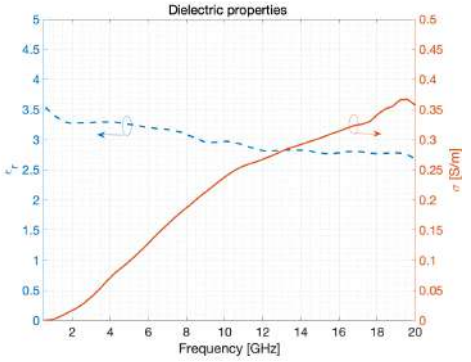

Fig. 4. Dielectric properties of hazelnut-cocoa cream.

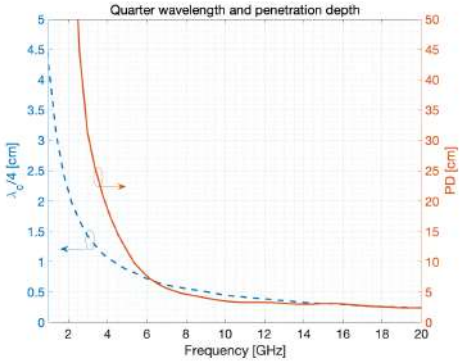

Fig. 5. Quarter wavelength and penetration depth within the hazelnut-cocoa cream.

B. Food Products and Frequency Range Selection

Microwave imaging techniques can be applied to penetrable materials whose losses, in the chosen working frequency range, allow back-scattered signals to be detected by the receiving antennas. Of course, the food packaging has to be transparent to microwaves: hence, we can apply the proposed microwave imaging system to non-metallic packaging only. Then, the choice of the working frequency range is strongly related to the dielectric properties and size of the food product under analysis, in particular to its conductivity and maximum dimension that has to be penetrated by microwaves. It is worth recalling that the operating frequency also influences the achievable spatial resolution of the imaging system [19].

In this work, we focus on standard-size glass jars filled with hazelnut-cocoa cream that, from a dielectric point of view, corresponds to oil. Hence, the following considerations can be easily generalized to any oil-based food product with similar packaging sizes. Moreover, hazelnut-cocoa cream can be reliably modeled as a homogeneous medium at microwave frequencies, which makes the application of a differential imaging approach (see Sect. II-A) to some extent easier. Hence, the variations of the dielectric contrast are mainly due to the presence of contaminants to be detected. However, we underline that the proposed approach can be investigated also in the case of packaged inhomogeneous food products, but this is outside the scope of the present work.

The electromagnetic properties of hazelnut-cocoa cream in the microwave frequency range have been measured with a coaxial dielectric probe immersed in the cream and connected to a VNA. The measured relative permittivity ϵ_r and conductivity σ are depicted in Fig. 4.

In order to choose the most appropriate microwave frequency range to image jars filled with hazelnut-cocoa cream, we evaluate, from the measured data shown in Fig. 4, the wavelength within the cream, λ_c, and the penetration depth (PD, distance where the EM radiation intensity inside the material is reduced by about 37%), both shown in Fig. 5. The $\lambda_c/4$ gives an indication of the expected spatial resolution of the implemented imaging algorithm, while the PD describes the effect of the dielectric losses on the intensity of the penetrating and backscattered waves. As evident from Fig. 5, if the frequency is higher, the resolution increases, conversely, there is a reduction of the wave penetration in the dielectric medium. As a trade-off between these two opposite requirements and considering that the jar diameter is 8-cm long, we choose a working frequency range around 10 GHz, where PD is equal to 3.5 cm and $\lambda_c/4$ to 4 mm (see Fig. 5). However, we would like to underline that, in the proposed application, it is not essential to identify the size of the contaminant, but simply to detect and localize it. Therefore, the main criterion is not the highest spatial resolution achievable with the imaging setup, but the lowest intensity of the field scattered by the contaminant that can be detected. As the intensity of the scattered field is proportional to the contaminant size, the detection level is linked both to the receiver sensitivity and to the contaminant size. Hence, this might lead to detect fragments smaller than the actual imaging algorithm spatial resolution, but this has to be verified experimentally with the chosen receiver.

III. 2-D Concept Validation

To validate the proposed system, we initially consider a simplified 2-D scenario, which allows to perform fast and easy-readable numerical tests. The considered geometry is shown in Fig. 3; the jar, filled with hazelnut-cocoa cream, is modeled as an infinite dielectric circular cylinder with diameter equal to 8 cm, and each of the 26 antennas (13 antennas for each side of the line) is modelled with an infinite current wire parallel to the jar. According to the analysis in Sect. II-B, the chosen frequency range is $9-11$ GHz sampled with 9 evenly spaced frequency points. The SVD truncation index T in (2) is chosen according to the distribution of the singular values σ_n and considering a signal-to-noise ratio (SNR) of 70 dB. Hence, in order to keep enough right singular vectors $[v_n]$ in (2), to properly reconstruct the contrast variation $[\Delta\chi]$, and, on the other side, to limit the noise, we set an SVD threshold of -30 dB that corresponds to $T = 82$.

The first analyzed aspect is how the designed system is able to probe (and image) the domain of interest D. To this end, we observe the *spatial coverage* of the operator $\mathbb{S}$ [20], which is defined as

$$s\left(\boldsymbol{r}_m\right) = \frac{\sum_{n=1}^{T} \left|v_n\left(\boldsymbol{r}_m\right)\right|^2}{\max\limits_{\boldsymbol{r}_m \in D} \left[\sum_{n=1}^{T} \left|v_n\left(\boldsymbol{r}_m\right)\right|^2\right]}, \tag{3}$$

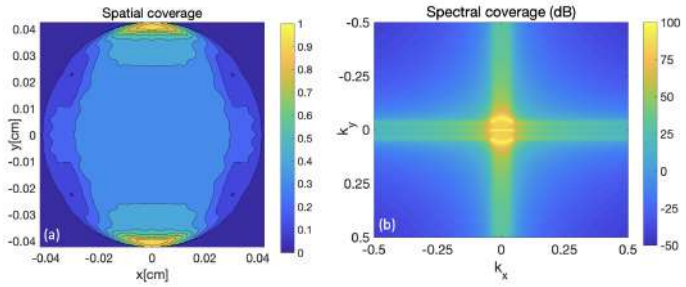

Fig. 6. (a): spatial coverage s; (b): spectral coverage $\tilde{s}$ (dB); $T = 82$.

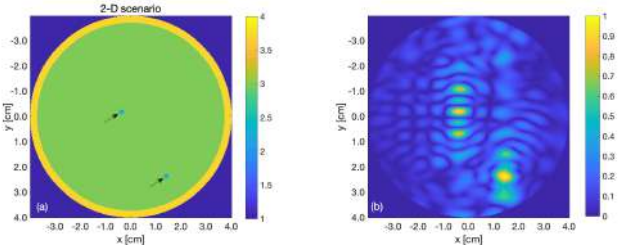

Fig. 7. (a): 2-D scenario geometry with 2 PLA fragments; (b): reconstructed tomographic image.

where $v_n(\boldsymbol{r}_m)$ is the m-th element of the n-th right singular vector in (2), evaluated in $\boldsymbol{r}_m \in D$. For the considered working conditions, the obtained spatial coverage, $s(\boldsymbol{r}_m)$, is shown in Fig. 6.(a), demonstrating an overall good capability of probing the domain under test: only on the two jar sides, orthogonal to the line, the coverage is lower, but not null.

Additional information can be obtained from the *spectral coverage* of the scattering operator $\mathbb{S}$ [21], defined as

$$\tilde{s}(\boldsymbol{k}_m) = \sum_{n=1}^{T} |F[v_n(\boldsymbol{r}_m)]|^2, \tag{4}$$

where $F[\cdot]$ is the 2-D discrete Fourier Transform operator (shifting the zero-frequency component to the center of the spectrum), and $\boldsymbol{k}_m$ is the m-th point location in the spectral domain corresponding to $\boldsymbol{r}_m$ in the spatial one. Figure 6.(b) shows the spectral coverage, which confirms the capability of resolving targets along the x direction thanks to the use of the synthetic aperture, while reveals a limited coverage in k_y, due to the fact that the antennas are located on two sides only. This will result in the presence of replicas along the y direction in the reconstructed contrast, which however do not impair the effective detection of the contaminant.

To confirm the above observations, we simulated the case in which two contaminants with diameter equal to 2 mm are present within the jar. This corresponds to the minimum contaminant size detectable by XRI systems for packaged food monitoring. The contaminants are made of polylactide (PLA) plastic ($\epsilon_r = 2.3$, negligible losses). Note that this kind of low-density plastic fragments are not easily detectable by XRI systems. The overall scenario is summarized in Fig. 7.(a): the external part is air ($\epsilon_r = 1$), the jar is filled with hazelnut-cocoa cream (see ϵ_r and σ in Fig. 4), the jar walls are made of glass with thickness equal to 3 mm, ($\epsilon_r = 3.7$ and negligible losses), and the two inner dots are the two PLA contaminants ($\epsilon_r = 2.3$). Figure 7.(b) shows the microwave tomographic image obtained by applying (2) to the simulated data with added SNR = 70 dB. The image displays the normalized amplitude of the estimated $\Delta\chi$. The two contaminants are properly detected but, as expected, with some replica along the y direction.

IV. 3-D Validation in Controlled Conditions

In this section, we present some experimental tests performed in an intermediate scenario, before the final industrial setting. In this validation, we recreated the same scenario as in the final experiment, emulating the presence of the moving belt. To this end, measurements are taken by manually changing the relative position of the jar with respect to the antennas pair to emulate the movement. Before performing measurements, a full-fledged 3-D simulation of the experiment has been carried out to both foresee the system capabilities and interpret the experimental imaging results.

A. 3-D Simulations

Figure 8 depicts the simulated experimental scenario in which a pair of wide-band dual-ridged horn antennas is positioned parallel to the virtual belt, along the jar axis movement, at 2 cm from the jar [see Fig. 8.(a)].

The simulated scattering parameters are computed for each jar position with and without the contaminant inside, to provide the differential $[\Delta S]$ data. As for the 2-D set-up, 13 jar positions are considered, where, each time, the jar moves forward 1 cm. The contaminant is now a metallic sphere with radius equal to 5 mm. The reported results are simulated at 10 GHz.

Figure 9 depicts the 3-D reconstructed tomographic images obtained from the simulated data, where the reference scenario is shown in the first row. In the second row, the results obtained using mono-static and bi-static data are reported. As for the 2-D case, in the xz plane [see Fig. 9.(f)] the contaminant is well identified with some replica along the x axis, that is orthogonal to the movement direction (z axis). Moving to the yz plane [see Fig. 9.(h)], while we can correctly image the target along the z axis thanks to the synthetic aperture, the lack of measurements taken at different values of the y axis prevents to discriminate targets along this direction. In particular, we observe a pair of specular targets along the

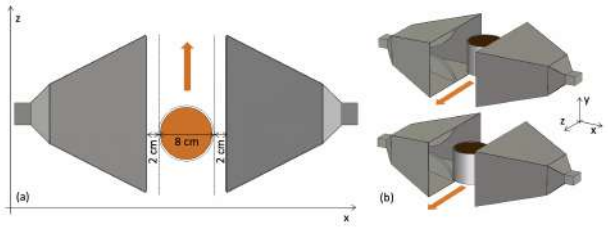

Fig. 8. Simulated 3-D scenario; (a): xz view with geometrical dimensions; (b): 3-D view at different time instants.

y axis because the near-field pattern radiated by the adopted antennas in the yz plane is not homogeneous and exhibits two peaks at the extremities of the y axis, as shown in Fig. 10.(b). Finally, the image in the xy plane is affected by all of the issues mentioned above [see Fig. 9.(g)], and the corresponding antenna radiated near field is shown in Fig. 10.(a).

The third row of Fig. 9 reports the reconstruction when only bi-static data are used in (2), i.e., the self terms $\Delta S_{p,p}$ and $\Delta S_{q,q}$ are discarded. In this case, the contaminant is still identified, but the reconstructions are fully symmetrical with respect to the plane between the two antennas apertures (yz plane). Such an outcome is due to the fact that using only bi-static measurements, the optical paths Tx-target-Rx and received signals are the same by virtue of reciprocity, while mono-static data convey the information about the jar side where the contaminant is located.

B. Measurements

The experimental set-up is shown in Fig. 11: two wide-band dual-ridged horn antennas are placed opposite each other, with a wooden support in the middle where the jar filled with hazelnut-cocoa cream is placed. The two antennas are connected through coaxial cables to the VNA ports (Keysight N5227A, IF = 500 Hz, nominal input power) to measure the scattering parameters. The measurements are performed inside an anechoic chamber to reduce external interferences. The jar is positioned at 13 different positions, mimicking the sampling as in the real case. As in the simulations, the contaminant is a metallic sphere with radius equal to 5 mm.

As evident in Fig. 11.(b), some inaccuracies are present in the measurement set-up. Firstly, the jar movement is done manually, and, even if it is done with the help of a hand-made positioner, this implies inaccuracies in the relative positioning of the jar with respect to the antennas. These positioning inaccuracies have an impact on the accuracy of measured differential scattering parameters, $[\Delta S]$, which assume that the jar without contaminant (i.e. the "reference" jar) and the one with the contaminant inside are placed in the same locations. Moreover, they introduce a model error in the discretized scattering operator, $[\mathbb{S}]$, to be used in (2), where the relative position between the jar and the antennas has to be specified. Secondly, the expected contaminant position is not exactly known, mainly because the background medium is the hazelnut-cocoa cream, whose opacity does not allow to see where the contaminant is exactly located.

Figure 12 shows the 3-D reconstructed tomographic image obtained from measured data at 10 GHz. The first row reports the expected contaminant position within the jar under different views, while the second row shows the tomographic images. Similar to what happened with the synthetic data (see Fig. 9), the contaminant is properly identified, but with replicas along the x axis. Moreover, the obtained reconstructions are fully symmetrical with respect to the yz plane, because only measured bi-static data are used. The measured mono-static data, i.e., the self terms $\Delta S_{p,p}$ and $\Delta S_{q,q}$, were discarded because the two antennas are not perfectly identical and the scenario is not fully symmetrical, even when the contaminant is not present. Mono-static data could be recovered via a proper calibration, but this is outside the scope of this work.

Finally, the last row of Fig. 12 shows the 3-D reconstructed tomographic images obtained from the subtraction of two sets of measured scattering parameters acquired with uncontaminated jars. The reconstructed images are normalized with respect to the maximum reconstructed value in the presence of the contaminant (i.e. data shown in the second row of Fig. 12). It is evident that, despite the inaccuracies in the measurement set-up, the tomographic image without contaminants exhibits quantitative values significantly lower than the ones with the contaminant: this test is very important for industrial applications because, obviously, false-positive detection must be avoided.

In addition to the reported reconstructed images, in the following we investigate some metrics made directly on the measured scattering parameters, obviously affected by the presence of the contaminant within the jar, that can be useful to support the user interpretation of the tomographic images, in parallel with an image analysis procedure.

The first considered metric is the 2-norm (or Euclidean norm) of the differential scattering vector, $||\,[\Delta S]\,||_2$; it is expect to be ideally zero if the difference between two jars without contaminants is considered, and greater than zero if one of the two considered jars contains a contaminant while the other does not. In fact, when a contaminant is present, $[\Delta S]$ is relative to the field scattered by the contaminant, while if there are no contaminant, it only reflects the effect of noise and position uncertainties. The first row of Table I reports the $||\,[\Delta S]\,||_2$ values obtained with the measured scattering parameters at 10 GHz in the case of two jars without contaminants (second column labelled as "Empty") and in the case when the contaminant is present in only one jar (third column labelled as "Contaminant"). As expected, the 2-norm increases if the contaminant is present.

Another considered metric is based on the "similarity" between the scattering parameters measured with and without the contaminant. The assumption is that the presence of the contaminant should substantially affect the measured scattering parameters, while two cases without contaminants should be very similar (ideally identical). Moreover, there should be more diversity in the measured scattering parameters when a contaminant is present. In order to estimate the level of similarity, the Pearson's linear correlation coefficient ρ is

TABLE I
ANALYZED DATA METRICS IN VIRTUAL MOVEMENT MEASUREMENTS.

Virtual movement measurements	Empty	Contaminant
$\|\|\,[\Delta S]\,\|\|_2$, 10 GHz	0.0169	0.0502
ρ_{p}, 10 GHz	0.9995	0.9956
$\bar{\rho}_{\mathrm{p}}$, 8-12 GHz (201 points)	0.9992	0.9960
σ_{p}, 8-12 GHz (201 points)	$3.7\ 10^{-4}$	$1.6\ 10^{-3}$
$\bar{\rho}_{\mathrm{f}}$, 13 positions	0.9990	0.9915
σ_{f}, 13 positions	$1.3\ 10^{-3}$	$8.3\ 10^{-3}$

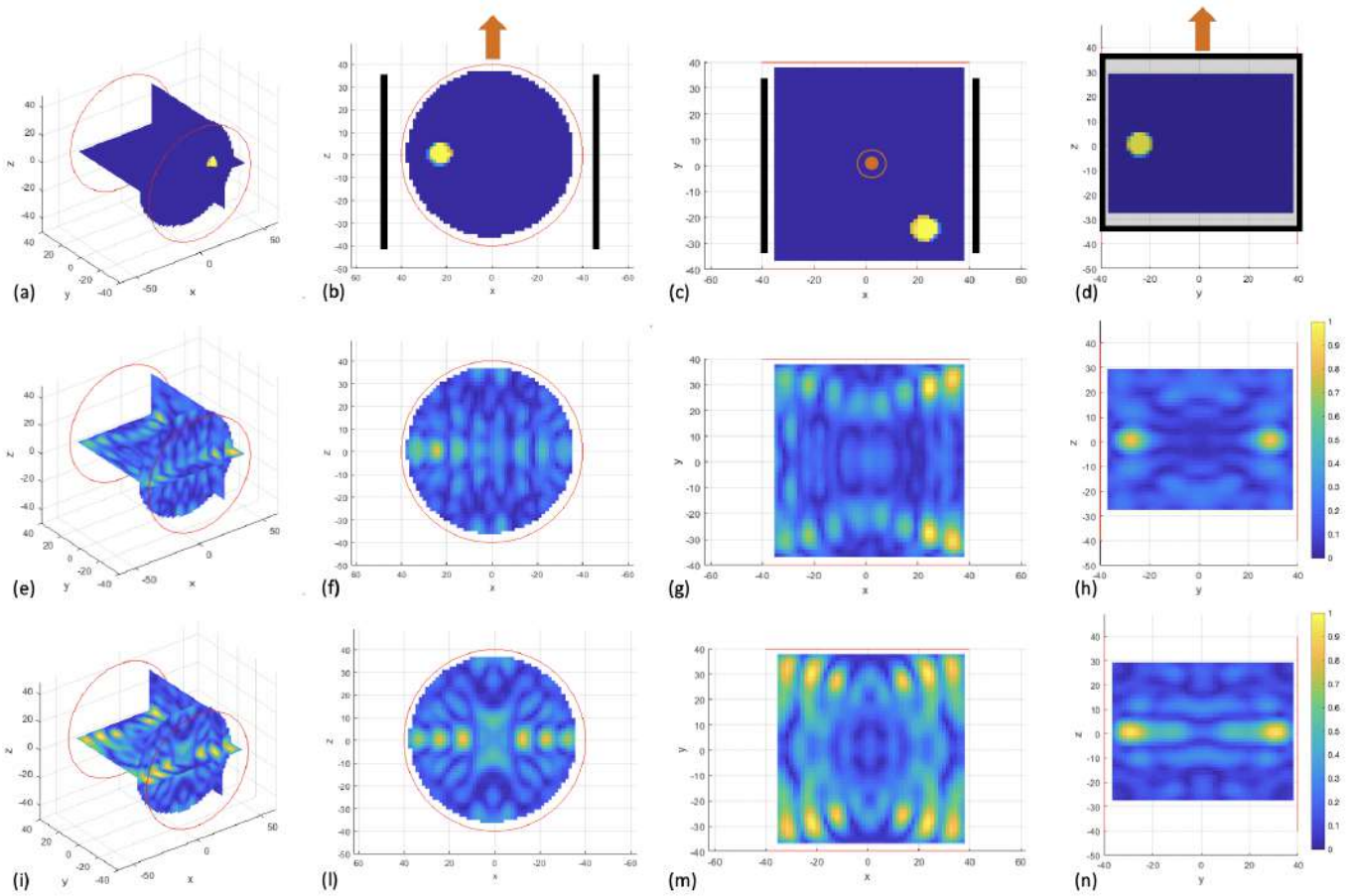

Fig. 9. Synthetic data results; (a)-(d): 3-D permittivity contrast in the reference scenario; (e)-(h): 3-D reconstructed tomographic images using mono- and bi-static data; (i)-(n): reconstructed ones using bi-static data only. Each column corresponds to a different view; in the first row the two horn antennas are reported in black and the jar movement is highlighted with orange arrows; all the geometrical units are in mm.

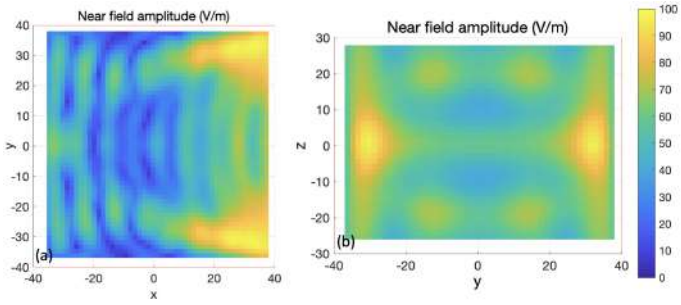

Fig. 10. Near field radiated by one of the adopted dual-ridged horn antennas in the xy and yz planes in front of the antenna aperture; the planes are selected where the contaminant is located.

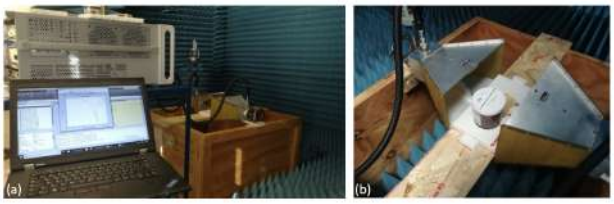

Fig. 11. System set-up for virtual movement measurements; (a): whole system; (b): close-up of the two antennas together with the jar.

evaluated between several measured signals [22]. First of all, the scattering parameters measured at 10 GHz in the 13 jar positions have been correlated: the obtained coefficient, ρ_{p}, is reported in the second row of Table I. As expected, ρ_{p} is lower when the contaminant is present. Then, the correlation coefficients ρ_{p} have been evaluated from 8 to 12 GHz as shown in Fig. 13.(a). In the whole frequency range, the correlation between the measured scattering parameters is lower when the contaminant is present. The average over frequency of the evaluated position correlation coefficients, $\bar{\rho}_{\mathrm{p}}$, is reported in third row of Table I, along with its standard deviation, σ_{p} (fourth row of Table I), which is higher in presence of the contaminant. A similar analysis is reported in Fig. 13.(b) where, instead, the correlation coefficients are evaluated at different jar (or antenna pair) positions between two sets of scattering parameters measured from 8 to 12 GHz (201 sample frequency points). The corresponding correlation coefficient, averaged on the 13 positions, $\bar{\rho}_{\mathrm{f}}$, and standard deviation, σ_{f}, are reported in the fifth and sixth rows of Table I, respectively. Such an analysis thus makes it possible to identify the presence of the contaminant which will result in a higher norm, a lower correlation coefficient and a higher associated standard deviation.

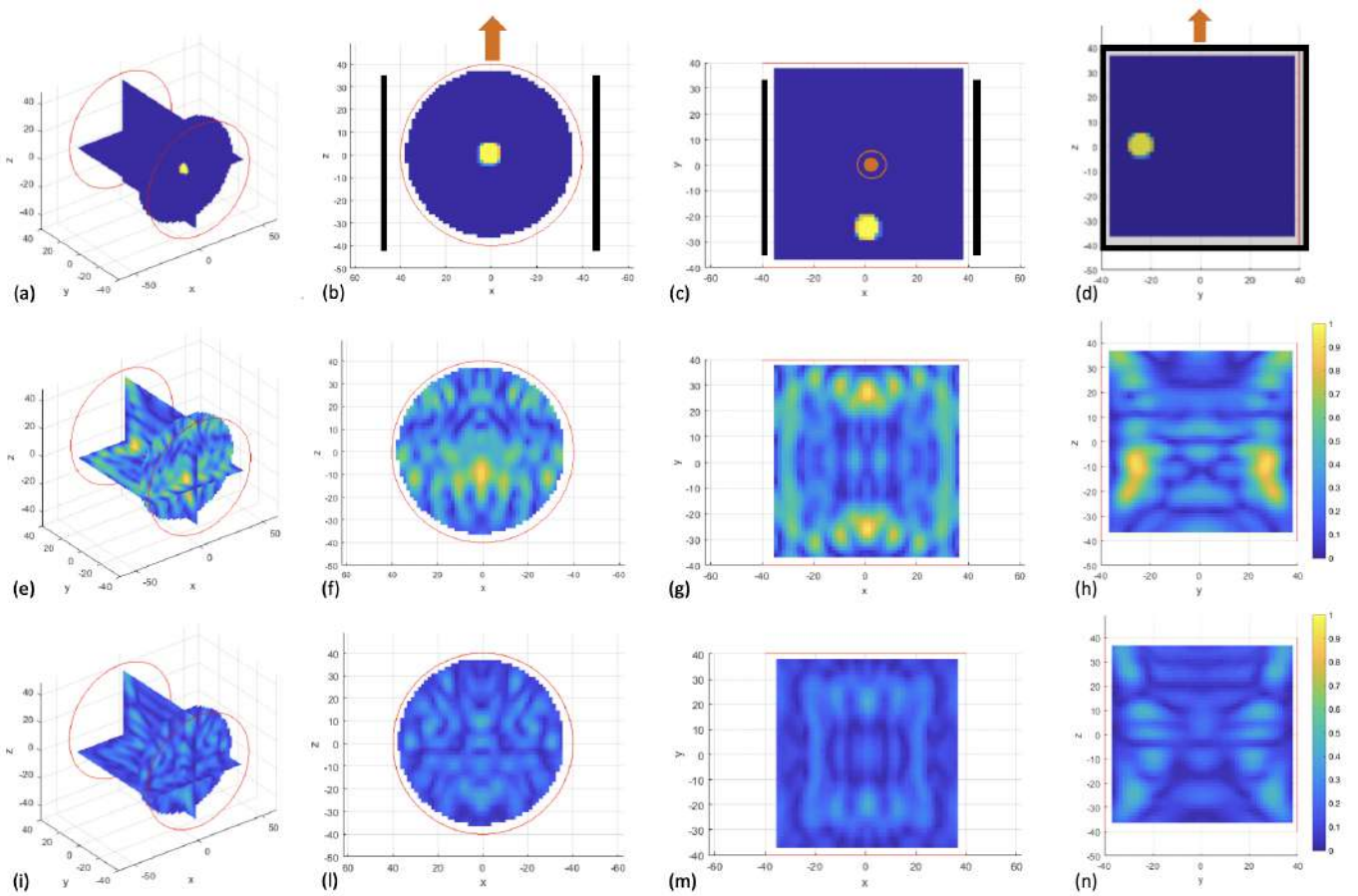

Fig. 12. Measurement data results; (a)-(d): 3-D reference scenario; (e)-(h): 3-D reconstructed tomographic images obtained using bi-static data only; (i)-(n): reconstructed one obtained while subtracting two sets of data acquired with uncontaminated jars. Each column corresponds to a different view; in the first row the two horn antennas are reported in black and the jar movement is highlighted with orange arrows; all the geometrical units are in mm.

V. Preliminary Measurements in Movement

In this section, we describe a preliminary test of the proposed system in an actual operating environment. Although no imaging results have yet been achieved, the test is worth to be presented as it confirmed the feasibility of the approach and allowed us to identify some issues that must be taken into account to apply the tomographic approach when dealing with items moving on an actual conveyor belt. The measurement campaign has been performed at Nutkao s.r.l. facilities, using a conveyor belt with controlled speed. The measurement set-up in shown in Fig. 14.(a). The two wide-band dual-ridged horn antennas are placed on the two sides of the conveyor belt and connected via coaxial cables to the two ports of a portable VNA (Keysight P9375A, IF = 500 Hz, nominal input power), placed under the belt. The speed of the conveyor belt is 14 cm/s, around $1/3$rd of the velocity of a production line. The 2×2 scattering matrices are measured from 8 to 12 GHz (5 sample frequency points) every 52 ms, which corresponds to a jar lateral movement of 0.73 cm.

Figure 15.(a) shows sets of $|S_{21}|$, measured at 10 GHz, in different time instants when the same jar is passing between the two antennas. First of all, it is evident that the measured signals are not well synchronized, because the synchronization between the jar movement on the belt and the measurement acquisition is done manually. To overcome such an issue and improve the synchronization, a photocell system connected to the VNA external trigger has to be added, but, unfortunately, it was not available during the measurement campaign, so that the measured signals synchronization is done a posteriori by simply picking and aligning the maximum value on all the measurements, as shown in Fig. 15.(b). The implemented "max" synchronization allows to properly perform the metrics' analysis described in Sect. IV-B, but it is not sufficient to apply the imaging procedure. Indeed, information on the relative position between the jar and the antennas are needed for computing the discretized version of the scattering operator $[\mathbb{S}]$, and moreover it influences the phase of the data. Hence, in the following, only the metrics on the measured scattering parameters are reported.

In Fig. 15, a periodic ripple of about 1 dB is present when the jar is not close to the antennas. This effect is due to the small metallic joints which are periodically inserted in the conveyor belt. As a result, in the measurements, we have been careful to position the jar always in the same place with respect to the joints in order to limit their effects on the scattering data. It is worth noting that using an all-plastic conveyor belt, as in production lines where a metal detector is in place, would eliminate these ripples.

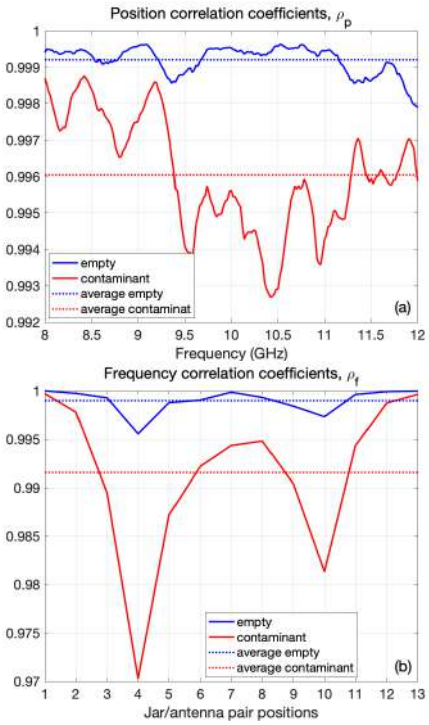

Fig. 13. Correlation coefficients of virtual movement measurements; (a): position correlation coefficients ρ_{p} versus frequency; (b): frequency correlation coefficients ρ_{f} versus jar / antenna pair positions. The average values $\bar{\rho}_{\mathrm{p}}$ and $\bar{\rho}_{\mathrm{f}}$ are shown with dotted lines.

Fig. 14. System set-up for measurements with jars in movement; (a): horn antennas and conveyor belt; (b): example of a contaminant within the hazelnut-cocoa cream jar; (c): considered plastic contaminants.

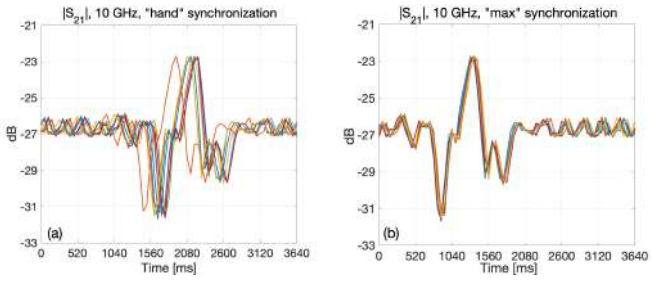

Fig. 15. $|S_{21}|$ measured at 10 GHz versus time; (a): before synchronization; (b): after synchronization.

TABLE II
DATA METRICS FOR MEASUREMENTS IN MOVEMENT.

	Empty	Metal	Plastic A	Plastic B
$\|\|\,[\Delta S]\,\|\|_2$, 10 GHz	0.0165	0.0405	0.0259	0.0288
ρ_{p}, 10 GHz	0.9888	0.9762	0.9835	0.9803
$\bar{\rho}_{\mathrm{p}}$, 8-12 GHz	0.9874	0.9702	0.9808	0.9772
σ_{p}, 8-12 GHz	$3.9\ 10^{-3}$	$11.3\ 10^{-3}$	$6.6\ 10^{-3}$	$7.3\ 10^{-3}$
$\bar{\rho}_{\mathrm{f}}$, 21 positions	0.9970	0.9893	0.9954	0.9946
σ_{f}, 21 positions	$2.4\ 10^{-3}$	$7.7\ 10^{-3}$	$3.9\ 10^{-3}$	$4.0\ 10^{-3}$

In the evaluation of the data metrics, the measurement time window is set to around 1 s, which corresponds to sampling the movement of the jar at 21 positions over a distance of around 15 cm, resulting in measurement conditions similar to those of the virtual movement set-up (see Sect. IV-B). The obtained data metrics are summarized in Table II, where four cases are considered: measurement without contaminants (second column), with a metal sphere contaminant as the one used in the controlled environment measurements (third column), and with two plastic fragments (forth and fifth columns), shown in Fig. 14.(b)-(c).

Comparing the obtained metrics with the ones in Table I, we can notice that, in the case without contaminants, all the metrics have similar values except for ρ_{p} and its average $\bar{\rho}_{\mathrm{p}}$, where the values obtained with the real jar movement are lower. This is possibly due to the not optimal synchronization of the measured signals. However, if the reference measurement (i.e. jar without contaminant) at the different jar positions is correlated with the ones with a contaminant inside the jar (last three columns of Table II) a reduction of ρ_{p} is still present, as also shown in Fig. 16.(a).

The frequency correlation coefficients ρ_{f}, both without contaminants and with a metallic contaminant (second and third columns of Table II, respectively), are quite similar to those of the controlled experiment, even though external interferences are now present (the measurement system is not shielded and is located in a harsh environment). This is confirmed also in Fig. 16.(b) that has the same ρ_{f} range as in the controlled validation [see Fig. 13.(b)]. Finally, as expected, in the case of plastic contaminants, the ρ_{p} and ρ_{f} coefficients are higher than the corresponding ones obtained with the metallic contaminant, but are still distinguishable from the case without contaminants.

VI. Conclusion and Perspectives

In this work we presented the design, realization and testing of an MWI system for detecting contaminants in packaged food products, focusing on hazelnut-cocoa cream jars. A progressive analysis has been presented, starting with a simplified 2-D simulated scenario up to an industrial measurement campaign. To process the data, a microwave tomography approach and the analysis of some suitable data metrics have been adopted. This allows to both perform detection of contaminants within food products by exploiting a classification framework based on the proposed metrics, as well

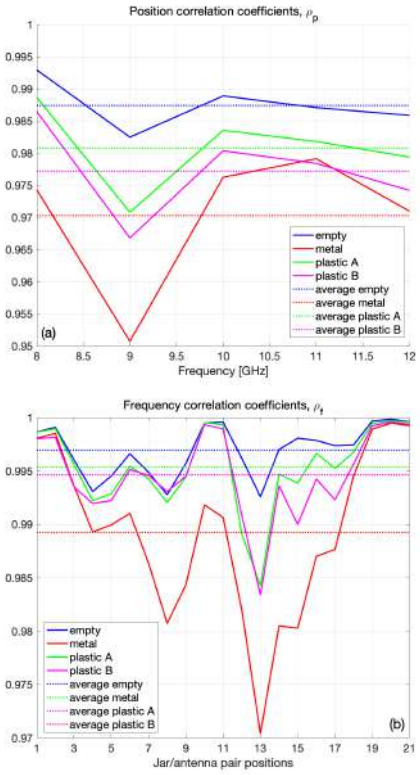

Fig. 16. Correlation coefficients of measurements in movement; (a): position correlation coefficients ρ_{p} versus frequency; (b): frequency correlation coefficients ρ_{f} versus jar / antenna pair positions. The average values $\bar{\rho}_{\mathrm{p}}$ and $\bar{\rho}_{\mathrm{f}}$ are shown with dotted lines.

as to take advantage of the imaging results to localize the contaminant, which is important to understand at which point of the production the issue might have occurred and therefore implement proper mitigation strategies. While the proposed MWI system has been designed for low-loss food products, the underlying technology is viable also for inspecting wet food, provided that the system specifications are updated using a similar analysis as the one performed in this work.

As this study presents a concept validation, there are of course several avenues for improvement. First of all, an automated synchronization of the measurements acquisition and the jar movement on the conveyor belt is needed. Such a synchronization would allow to both improve the evaluated metrics and implement the imaging algorithm in a realistic environment. Moreover, other metrics can be investigated to better detect the presence of the contaminant. Finally, an interesting opportunity is offered by the implementation of an automated classification framework based on the proposed metrics by means of machine learning techniques [23], [24]. As a matter of fact, these powerful processing tools appear very appropriate, because large data sets can be easily available by performing continuous measurements along the conveyor belt. To this end, extensive measurement campaigns at industrial facilities are needed to confirm the first findings presented here, promote new ones, and to move from a prototype system to a commercial one.

ACKNOWLEDGMENT

We would like to thank Nutkao S.r.l. for providing the conveyor belt as well as the testing food products. Moreover, we acknowledge the valuable help of Eng. G. Dassano for the realization of the system for the controlled validation.

REFERENCES

[1] W.-H. Lee and W. Lee, "Food inspection system using terahertz imaging," *Microwave and Optical Technology Letters*, vol. 56, no. 5, pp. 1211–1214, 2014.

[2] K. Wang, D.-W. Sun, and H. Pu, "Emerging non-destructive terahertz spectroscopy imaging technique: Principle and applications in the agri-food industry," *Trends in Food Science & Technology*, vol. 67, pp. 93–105, 2017.

[3] C. Jordens and M. Kock, "Detection of foreign bodies in chocolate with pulsed THz spectroscopy," *Optical Engineering*, vol. 47, no. 3, pp. 93–105, 2008.

[4] [Online]. Available: http://terasense.com/applications/terahertz-food-inspection/

[5] Z. Wu and H. Wang, "Microwave tomography for industrial process imaging: Example applications and experimental results," *IEEE Antennas and Propagation Magazine*, vol. 59, no. 5, pp. 61–71, 2017.

[6] M. Asefi, I. Jeffrey, J. LoVetri, C. Gilmore, P. Card, and J. Paliwal, "Grain bin monitoring via electromagnetic imaging," *Computers and Electronics in Agriculture*, vol. 119, pp. 133–141, November 2015.

[7] [Online]. Available: http://www.foodradar.com/

[8] M. Butchers, M. Littlewood, and S. Baty, *UK Sensing Technologies for Contamination in Food*. Sensors & Instr. Group, 2013.

[9] O. Schimmer et al., "UWB-sensors in food quality management: the way from the concept to market," in *Proc. IEEE Int. Conf. on Ultra-Wideband*, 2008.

[10] M. Edwards, *Detecting foreign bodies in food*. Woodhead Publishing Ltd, 2004.

[11] L. Farina et al., "In-line monitoring of food contamination via microwave imaging," in *Proc. 18th Mediterranean Microwave Symp.*, Nov. 2018.

[12] ——, "A feasibility study of a microwave imaging device for in-line food contamination monitoring," in *Proc. 13th European Conference on Antennas and Propagation*, Apr. 2019.

[13] Jorge A. Tobon Vasquez et al., "Monitoring of food contamination via microwave imaging," in *Proc. International Applied Computational Electromagnetics Society Symposium*, Apr. 2019.

[14] L. Farina et al., "Microwave imaging technology for in-line food contamination monitoring," in *Proc. IEEE International Symposium on Antennas and Propagation*, July 2019.

[15] Keysight Technologies, "Keysight streamline series USB vector network analyzer P937XA 2-port, up to 26.5 GHz," *Data Sheet*, Oct. 2018.

[16] R. Scapaticci, J. A. Tobon Vasquez, G. Bellizzi, F. Vipiana, and L. Crocco, "Design and numerical characterization of a low-complexity microwave device for brain stroke monitoring," *IEEE Trans. Antennas Propag.*, vol. 66, pp. 7328–7338, Dec. 2018.

[17] Jorge A. Tobon Vasquez et al., "Design and experimental assessment of a 2D microwave imaging system for brain stroke monitoring," *Int. J. Antennas Propag.*, no. Article ID 8065036, p. 12 pages, 2019.

[18] M. Bertero and P. Boccacci, *Introduction to Inverse Problems in Imaging*. Inst. Phys., Bristol, U.K., 1998.

[19] M. Slaney, A. C. Kak, and L. E. Larsen, "Limitations of imaging with first-order diffraction tomography," *IEEE Transactions on Microwave Theory and Techniques*, vol. 32, no. 8, pp. 860–874, Aug. 1984.

[20] R. Scapaticci, V. Lopresto, R. Pinto, M. Cavagnaro, and L. Crocco, "Monitoring thermal ablation via microwave tomography: An ex vivo experimental assessment," *Diagnostics*, vol. 8, no. 4, 2018. [Online]. Available: https://www.mdpi.com/2075-4418/8/4/81

[21] G. Leone and F. Soldovieri, "Analysis of the distorted born approximation for subsurface reconstruction: truncation and uncertainties effects," *IEEE Transactions on Geoscience and Remote Sensing*, vol. 41, no. 1, pp. 66–74, Jan 2003.

[22] SPSS tutorials: Pearson correlation. [Online]. Available: https://libguides.library.kent.edu/SPSS/PearsonCorr

[23] A. Massa, G. Oliveri, M. Salucci, N. Anselmi, and P. Rocca, "Learning-by-examples techniques as applied to electromagnetics," *J. of Electromagnetic Waves and Applications*, vol. 32, no. 4, pp. 516–541, 2018.

[24] A. Massa et al., "Dnns as applied to electromagnetics, antennas, and propagation—a review," *IEEE Antennas and Wireless Propagation Letters*, vol. 18, no. 11, pp. 2225–2229, 2019.